Northumbria Research Link

University**Library**

On the Relative Strength of Electric and Magnetic ULF Wave Radial Diffusion During the March 2015 Geomagnetic Storm

L. Olifer[1] [ID], I. R. Mann[1] [ID], L. G. Ozeke[1] [ID], I. J. Rae[2] [ID], and S. K. Morley[3] [ID]

[1]Department of Physics, University of Alberta, Edmonton, Alberta, Canada, [2]Mullard Space Science Laboratory, Department of Space and Climate Physics, University College London, London, UK, [3]Space Science and Applications, Los Alamos National Laboratory, Los Alamos, NM, USA

Abstract In this paper, we study electron radial diffusion coefficients derived from Pc4-Pc5 ultralow frequency (ULF) wave power during the intense geomagnetic storm on 17–18 March 2015. During this storm the population of highly relativistic electrons was depleted within 2 hr of the storm commencement. This radial diffusion, depending upon the availability of source populations, can cause outward radial diffusion of particles and their loss to the magnetosheath, or inward transport and acceleration. Analysis of electromagnetic field measurements from Geostationary Operational Environment Satellite (GOES), Time History of Events and Macroscale Interactions during Substorms (THEMIS) satellite, and ground-based magnetometers shows that the main phase storm-specific radial diffusion coefficients do not correspond to statistical estimates. Specifically, during the main phase, the electric diffusion (D_{LL}^E) is reduced, and the magnetic diffusion (D_{LL}^B) is increased, compared to empirical models based on Kp. Contrary to prior results, the main phase magnetic radial diffusion cannot be neglected. The largest discrepancies, and periods of dominance of D_{LL}^B over D_{LL}^E, occur during intervals of strongly southward IMF. However, during storm recovery, both magnetic and electric diffusion rates are consistent with empirical estimates. We further verify observationally, for the first time, an energy coherence for both D_{LL}^B and D_{LL}^E where diffusion coefficients do not depend on energy. We show that, at least for this storm, properly characterizing main phase radial diffusion, potentially associated with enhanced ULF wave magnetopause shadowing losses, cannot be done with standard empirical models. Modifications, associated especially with southward IMF, which enhance the effects of D_{LL}^B and introduce larger main phase outward transport losses, are needed.

1. Introduction

After the discovery of relativistic (hundreds of kiloelectron volts to megaelectron volts) and ultrarelativistic (>2 MeV) electron populations, trapped in the magnetosphere of the Earth (Van Allen & Frank, 1959), understanding their dynamics has been a focus in the space physics (e.g., Friedel et al., 2002; Turner et al., 2013, and references therein). Processes of electron acceleration up to megaelectron volt energies during geomagnetic storms have been studied in great detail (e.g., Albert, 2005; Horne et al., 2005; Omura et al., 2007; Shprits et al., 2008; Thorne et al., 2013, to list a few), but many important questions remain. Meanwhile, the processes that can cause Van Allen radiation belt losses are also still hotly debated. According to the current theories, trapped particles can be lost downward to the atmosphere of the Earth, or outward across the magnetopause to the magnetosheath. The atmospheric loss usually involves interactions with high-frequency waves and scattering into the loss cone. Examples of waves that cause such an atmospheric loss are electromagnetic cyclotron waves (e.g., Kang et al., 2016; Kersten et al., 2014; Shprits et al., 2016), plasmaspheric hiss (e.g., Lee et al., 2013; Thorne et al., 1973), or chorus waves (e.g., Li et al., 2014; Shprits et al., 2007). Studies of Brito et al. (2015) and Rae et al. (2018) also suggested the possible role for electron scattering into the loss cone due to interactions with localized compressional ultralow frequency (ULF) waves. Meanwhile, outward shadowing losses through the magnetopause can be enhanced by outward diffusion due to interactions with ULF waves (e.g., Loto'aniu et al., 2010; Mann & Ozeke, 2016; Mann et al., 2016; Shprits et al., 2006).

Recent long-term radiation belt simulations by Drozdov et al. (2017) suggest that EMIC wave losses, parametrized in their model using solar wind dynamic pressure, may be important. However, recent studies,

for example, by Olifer et al. (2018), have reemphasized the potential importance of magnetopause shadowing with outward electron transport through the last closed drift shell (LCDS). Olifer et al. (2018) showed how very fast losses, with timescales less than the Van Allen Probes orbital periods ($\sim$ 4 hr), can be explained by magnetopause shadowing. One such fast loss event was reported by Ozeke et al. (2017) for the September 2014 magnetic storm where similar to the Olifer et al. (2018) results fast radiation belt extinction was observed.

In this paper, we perform analysis of the ULF perturbations in the electromagnetic field of the Earth's magnetosphere, which could lead to outward ULF wave radial diffusion during the 17–18 March 2015 magnetic storm for which fast LCDS controlled losses were reported by Olifer et al. (2018). We derive the event-specific radial diffusion coefficient (D_{LL}) using data from Geostationary Operational Environment Satellite (GOES) and Time History of Events and Macroscale Interactions during Substorms (THEMIS) satellite as well as from the ground-based magnetometers. During this intense storm, we show that the event-specific radial diffusion coefficients do not correspond to those in *Kp*-dependent statistical models such as presented by Brautigam and Albert (2000) and Ozeke et al. (2014). Our results are similar to the ones obtained by Pokhotelov et al. (2016) for the October 2012 geomagnetic storm and by Dimitrakoudis et al. (2015) using analysis of 11 years of ground-based magnetometers data. Our results imply that performing the radial diffusion simulations with *Kp*-parametrization empirical models for D_{LL} can lead to an underestimation of the diffusion rates, especially during storm main phase.

2. Data and Methodology

In this section, we present an overview of the 17 March 2015 geomagnetic storm and describe the methodology, which we used to study the diffusion coefficients. We analyze in situ fields data from THEMIS (Angelopoulos, 2008) and GOES (Singer et al., 1996) satellites, as well as from multiple ground-based magnetometers, to calculate radial diffusion coefficients. The analysis is performed for 17–18 March 2015 during the main phase and early recovery phase of the storm.

2.1. Overview of the March 2015 Storm

Figure 1 shows a summary of selected solar wind parameters, geomagnetic indices, the 2.6 MeV radiation belt flux response measured by the Van Allen Probes, the 3 MeV flux observed by the Global Positioning System (GPS) constellation of satellites (e.g., Olifer et al., 2018), and the position of the LCDS on 17–18 March 2015. This event is often characterized as a radiation belt extinction event (e.g., Olifer et al., 2018) because of intensity and the short timescales of the outer radiation belt losses during the main phase. Solar wind parameters, as well as geomagnetic indices, were taken from the Operating Missions as a Node on the Internet (OMNI) database (King, 2005). Van Allen Probes energetic electron flux data were taken from National Aeronautics and Space Administration's (NASA's) Van Allen Probes database for the Relativistic Electron-Proton Telescope instrument (Baker et al., 2013). Following Olifer et al. (2018), the bottom panel of Figure 1 shows the energetic particle flux data measurement made by the GPS constellation with the Combined X-ray Dosimeter (CXD) (Morley et al., 2010, 2016; Tuszewski et al., 2004). These data have higher time resolution across L-shells above GPS altitudes than provided along the orbit trajectories of the NASA's Van Allen Probes and thus provides the potential to develop a more complete picture of radiation belt dynamics during periods of fast loss (Morley et al., 2010, 2017). Note that the *y* axis scale and limits of the two last panels are different.

The Van Allen Probes electron flux data show intense loss occurring between two subsequent orbits of the Probes on 17 March 2015 between around 06:00 and 10:00 UT, with further loss depleting the whole outer radiation belt until $\sim$18:00 UT on the same day. As discussed by Olifer et al. (2018), the orbital coverage of the Van Allen Probes does not allow electron dynamics on timescales of $\lesssim$1 hr to be resolved. However, combined data from 17 GPS satellites provide high ($\sim$30 min) temporal resolution and clearly show the pattern of the dropout. Note that the GPS satellites have a circular orbit with a radius of 4.2 Earth radii and thus can only observe L-shells above $L = 4.2$. Also, because the CXD instrument measures particles within a broad range of incidence angles, the measurements contain multiple pitch angles, capturing different parts of the pitch angle distribution on different L-shells (Morley et al., 2010; Tuszewski et al., 2004). Nonetheless, one still can examine the time dependence of the GPS electron flux data to characterize the dropout with high temporal resolution at each L (Olifer et al., 2018).
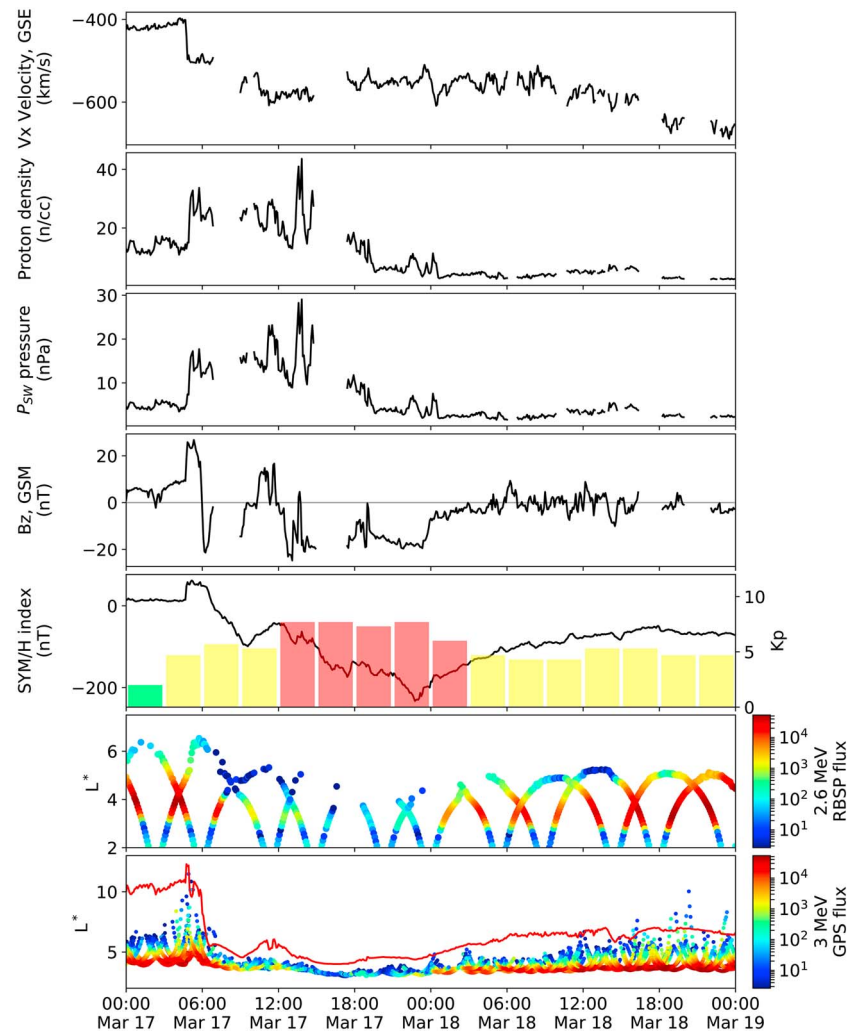
Figure 1. Summary of selected solar wind parameters and geomagnetic indices, 2.6 MeV, and 3 MeV radiation belt electron response during the 17–18 March 2015 geomagnetic storm. From top to bottom: solar wind velocity x component in GSE coordinates; solar wind proton number density; solar wind dynamic pressure; z component of the interplanetary magnetic field in GSM coordinates; geomagnetic SYM-H index as a line plot and Kp index as a bar plot; 2.6 MeV electron differential flux measured by the REPT instrument on the Van Allen Probes as a function of L^* and time in units of $cm^{-2} \cdot s^{-1} \cdot sr^{-1} \cdot MeV^{-1}$; and 3 MeV electron differential flux measured by the CXD instrument on the constellation of GPS satellites as a function of L^* and time in $cm^{-2} \cdot s^{-1} \cdot sr^{-1} \cdot MeV^{-1}$ overplotted with the position of the last closed drift shell from Olifer et al. (2018). GPS = Global Positioning System; GSE = geocentric solar ecliptic; RBSP = Radiation Belt Storm Probes; GSM = geocentric solar magnetospheric.

In Figure 1 the L^* values for the Van Allen Probes and GPS satellites, as well as the location of the LCDS, were calculated for the 90° pitch angle using the LANLmax and LANLstar algorithms (Yu et al., 2012) from the LANL* neural network provided by the SpacePy (Morley et al., 2011) python package. All of these calculations were made for the Tsyganenko and Sitnov (2005) magnetosphere model. Also, note that there are a small number of GPS electron flux measurements whose L^* is inferred to be above the LCDS, mostly toward the end of the UT day on 18 March. At this time these satellites were at high magnetic latitudes (∼ 60°) on the nightside, suggesting that this can be explained by uncertainties in the magnetic field model. A more detailed description of the GPS data and its comparison to the Van Allen Probes data and the LCDS during this event is presented in Olifer et al. (2018).

The interplanetary shock arrives at 03:40 UT on 17 March 2015. However, as discussed by Olifer et al. (2018), the GPS particle flux data does not show any signs of significant loss until 06:00 UT, when the interplanetary magnetic field (IMF) turns southward and the LCDS moves inward. This observation was used by Olifer et al. (2018) to argue that magnetopause shadowing dominated as a governing factor of the loss during this event.

The LCDS on 17 March 2015 also reaches low $L*$ down to $L* = 4$ and stays there for a relatively long period of ~5 hr. Presumably, this time is enough to deplete the heart of the radiation belt, for example, through fast outward ULF wave radial diffusion (e.g., Mann et al., 2016; Turner et al., 2012).

2.2. THEMIS Data

In this study, we used data from the three THEMIS satellites A, D, and E. In situ measurements of the magnetic field are taken from the triaxial fluxgate magnetometer experiment (Auster et al., 2008). Measurements of the electric field are taken from the electric field instrument (EFI; Bonnell et al., 2008). Both data sets are level 2 processed data and have 3 s resolution. ULF wave power spectral density (PSD), which is required to calculate the radial diffusion coefficients, can be obtained up to 167 mHz. Because we study ULF wave perturbations, the analysis of the PSD is performed for the frequency range from 1.2 to 20 mHz, which corresponds appropriately to Pc4–Pc5 waves. Electric and magnetic field data were provided by the Coordinated Data Analysis Web database in geocentric solar magnetospheric coordinates. However, the transformation of these data sets from geocentric solar magnetospheric to field-aligned coordinates (FACs) is required for our D_{LL} calculation. FACs were defined in the parallel direction by the background field, and in quasi-azimuthal (toroidal) direction using a vector perpendicular to the plane containing the background magnetic field and the geocentric radial vector to the spacecraft location. A quasi-radial (poloidal) vector completes the triad. For this purpose, the position of the THEMIS probes was taken from the Space Physics Data Facility (SPDF) Locator database. Meanwhile, the direction of the background magnetic field was calculated from in situ measurements for each of the probes after applying a running average with a 20 min window. The analysis created a negligibly small parallel component of the electric field at $L \geq 2$, validating the FAC approach.

The power spectral densities are calculated for the compressional component of the magnetic field ($B_\parallel$) and the quasi-azimuthal component of the electric field (E_ϕ) after applying a Hanning window with a total width of 40 min. The calculation of D_{LL} is performed only for L-shell range from 4.0 to 7.5, lower L-shell ranges introduce power that is aliased into the ULF band but derives from the rapid variation of the background magnetic field along the THEMIS orbit. Inbound and outbound passes of the THEMIS-A, THEMIS-D, and THEMIS-E probes cover time periods from around 11:00 UT until 20:00 UT for each day during March 2015 in the noon and dusk sectors. Note that the radiation belt loss happens between around 07:00 and 12:00 UT. Therefore, due to its orbital location, the in situ THEMIS data do not provide insight during the beginning of the storm. However, it still captures ULF wave characteristics in the later UT of the main phase as seen in Figure 1. The locations of the THEMIS satellites in the GSE X-Y plane are shown in Figure 2.

2.3. GOES Data

In addition to the THEMIS satellites, we used in situ measurements of the magnetic field from geosynchronous orbit, provided by the GOES-13 and GOES-15 satellites. The fluxgate magnetometer (Singer et al., 1996) measurements were obtained from the National Centers for Environmental Information National Oceanic and Atmospheric Administration database. The magnetometer data are provided with 512 ms resolution in spacecraft coordinates (see Fraser et al., 2013, for more details). Following the same procedure as for the THEMIS data, the magnetic field measurements are transformed into FAC, and the PSD of Pc4–Pc5 waves in the $B_\parallel$ component calculated along the whole orbit of the GOES-13 and GOES-15 satellites. Similarly to the THEMIS, the locations of the GOES satellites in the GSE X-Y plane are shown in Figure 2.

2.4. Ground-Based Magnetometer Data

We also use ground-based magnetometer data to estimate electric diffusion in the equatorial plane and compare this to the rates of diffusion estimated from GOES and THEMIS data. We use the mapping technique of Ozeke et al. (2009) to obtain equatorial quasi-azimuthal electric field E_ϕ from the magnetic east-west D-component of magnetic field on the ground. We use measurements of the magnetic field obtained by the CARISMA magnetometer array (Mann et al., 2008) and AUTUMN magnetometer array (Connors et al., 2016). In particular, we use the magnetometer data from Fort Smith (L=6.69) to obtain E_ϕ near GOES-13, and the magnetometer data from Inukjuak ($L = 6.91$) to obtain E_ϕ near GOES-15. Fort Smith magnetometer data are taken from the CARISMA website with 1 s resolution. Inukjuak magnetometer data are taken from the AUTUMN Virtual Magnetic Observatory website with 0.5 s resolution. Note that the assumed dipolar field line mapping (Ozeke et al., 2009) is most accurate on the dayside of the magnetosphere, and therefore, E_ϕ is obtained for magnetic local time between 06:00 and 18:00. This also removes the effects of nightside bags and other nightside or substorm processes with signatures in the Pc4–Pc5 ULF band for the ULF wave analysis. The footprints of the GOES satellites, as well as ground station locations, are shown in supporting
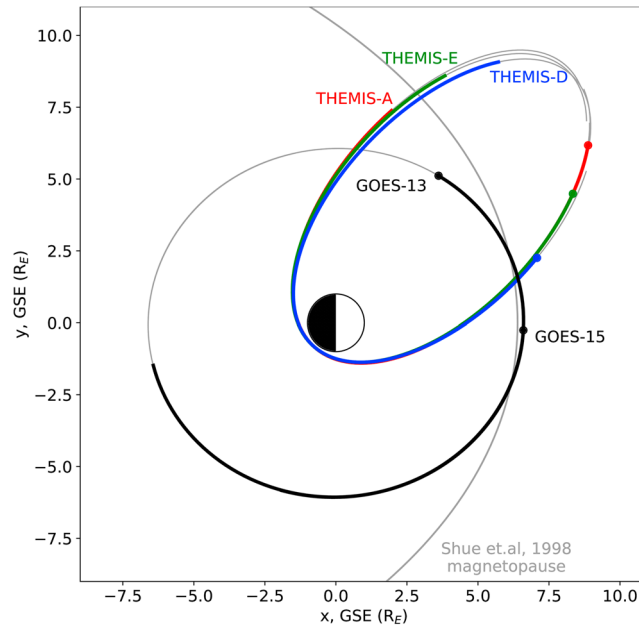
Figure 2. Orbits of the GOES and THEMIS satellites in the GSE *X-Y* plane during 17 March 2015. The orbit of THEMIS-A satellite is shown with red color, of THEMIS-D with blue, of THEMIS-E with green, and both GOES satellites are with black. Parts of the orbit from 10:00 until 21:00 UT shown in color the respective, meanwhile the remaining parts of the orbits are in gray. The round points represent the final position of the satellites at 21:00 UT on 17 March 2015. Additionally, we show the magnetopause location as calculated by Shue et al. (1998) empirical model for 8:30 UT on 17 March, where it is the closest to the Earth. THEMIS = Time History of Events and Macroscale Interactions during Substorms; GOES = Geostationary Operational Environment Satellite; GSE = geocentric solar ecliptic.

information Figure S1. Note that Fort Smith and Inukjuak magnetometers were selected as the closest magnetically conjugate stations to the GOES satellites during this storm, with the magnetic footprints calculated using the Tsyganenko and Sitnov (2005) magnetic field model. However, the Ozeke et al. (2009) technique used to map the ground magnetic fields into equatorial electric fields assumes a dipole magnetic field.

3. ULF Wave Radial Diffusion Coefficients

Depending on the direction of the radial gradient in phase space density, inward or outward radial diffusion of trapped particles in the radiation belt can be induced by ULF waves, especially those in the Pc4–Pc5 band with periods ranging from around 40 to 600 s or more. In particular, during periods of magnetopause shadowing (e.g., Turner et al., 2012) outward diffusion can enhance the subsequent loss of the particles through the magnetopause. Brizard and Chan (2001; see also Fei et al., 2006) derived relations for the radial diffusion coefficient (D_{LL}) as a function of the wave power, *P*, of perturbations in electric and magnetic fields. Fei et al. (2006) showed that the electric diffusion coefficient D_{LL}^E for electrons with drift frequency ω_d is given by equation (1a). The D_{LL}^E coefficient is proportional to the sum of wave powers $P_m^E\left(m\omega_d\right)$, where wave frequency ω satisfies the drift resonance condition $\omega = m\omega_d$ and where *m* is the azimuthal wave number. A similar proportionality to wave power also exists for magnetically induced diffusion, with diffusion coefficient D_{LL}^B (equation (1b)). Typically, the overall diffusion is assumed to be described by the sum of the two coefficients, providing the total diffusion coefficient for the system $D_{LL} = D_{LL}^E + D_{LL}^B$. As shown by Fei et al. (2006), these diffusion coefficients can be described in a dipole field by

$$D_{LL}^E = \frac{1}{8B_E^2 R_E^2} L^6 \sum_m P_m^E\left(m\omega_d\right), \tag{1a}$$

$$D_{LL}^B = \frac{M^2}{8q^2\gamma^2 B_E^2 R_E^2} L^4 \sum_m m^2 P_m^B\left(m\omega_d\right), \tag{1b}$$

where *M* is the first adiabatic invariant, *q* is the electron charge, γ is the relativistic gamma factor, B_E is the equatorial magnetic field strength at the surface of the Earth, R_E is the radius of the Earth, and *L* is the

L-shell. In our analysis, we use the dipole L-shells at the locations of the THEMIS and GOES satellites, as well as ground-based magnetometers, as input into the calculation of the diffusion coefficients. The latter was determined using the International Geomagnetic Reference Field model for 2015 (Thébault et al., 2015).

In later studies, Ozeke et al. (2014) simplified the assumed wave-particle interactions by only considering the first drift resonance mode ($m = 1$). The formulas for D_{LL}^E and D_{LL}^B derived by Ozeke et al. (2014) are shown in equations (2a) and (2b). Here, the angular drift frequency, ω_d, was substituted by the wave frequency f in above formulas (1), according to the drift resonance condition $\omega_d = \omega = 2\pi f$ for the assumed azimuthal wave number $m = 1$. We use these formulas to calculate the radial diffusion coefficients from in situ measurements from different satellites. Note that Ozeke et al. (2014) treat D_{LL}^E and D_{LL}^B as constant values, independent of wave frequency f (or particle energy, which defines ω_d) because of the assumption that the wave electric field PSD in the equatorial plane is frequency independent (as confirmed observationally by Brautigam, 2005, with Combined Release and Radiation Effects Satellite (CRRES) data) and that the magnetic field PSD decays as f^{-2}. However, in this study, we investigate characteristics of the frequency dependence of PSD and therefore the impact on the resulting diffusion coefficients during different phases of the magnetic storm. Therefore, we use the notation $D_{LL}^E(L, f)$ and $D_{LL}^B(L, f)$ to emphasize the frequency dependence of the radial diffusion coefficients. Also, keeping the notation introduced by Ozeke et al. (2014), we use P^E to represent the PSD of disturbances in the quasi-azimuthal component of the electric field, and P^B to represent the PSD in the compressional component of the magnetic field:

$$D_{LL}^E(L, f) = \frac{L^6}{8 B_E^2 R_E^2} P^E(L, f), \tag{2a}$$

$$D_{LL}^B(L, f) = \frac{L^8 4\pi^2}{9 \times 8 B_E^2} P^B(L, f) f^2. \tag{2b}$$

Additionally, Ozeke et al. (2014) obtained a *Kp*-parametrization of D_{LL}^E and D_{LL}^B given in equations (3a) and (3b), in units of day^{-1} as a function of *Kp* index and dipole L-shell. These formulas are commonly used in time-dependent radial diffusion simulations (e.g., Mann et al., 2016; Ozeke et al., 2017; Schiller et al., 2016). In this paper, we compare this *Kp*-parametrization of D_{LL} coefficients with the results obtained using in situ observations of the electric and magnetic fields during the 17–18 March 2015 intense geomagnetic storm. As discussed in detail below, we show that there is a strong discrepancy between the two especially during the main phase of the storm such that neither D_{LL}^B nor D_{LL}^E can be neglected as is traditionally assumed.

$$D_{LL}^E = 2.1 \cdot 10^{-8} L^6 10^{0.217 L + 0.461 K_P}, \tag{3a}$$

$$D_{LL}^B = 6.62 \cdot 10^{-13} L^8 10^{-0.0327 L^2 + 0.625 L - 0.0108 K_P^2 + 0.499 K_P}. \tag{3b}$$

4. Results

In this section, we calculate observationally constrained event-specific radial diffusion coefficients for the 17–18 March 2015 geomagnetic storm using in situ data from the GOES and THEMIS satellites. Note that the orbit of the Van Allen Probes lies in the magnetotail during this storm. Therefore, we do not present D_{LL} coefficients derived from the fields measured by the Van Allen Probes since they are located in stretched fields on the night side. Since the focus of this paper includes analysis of possible outward radial transport to the magnetopause during the main phase of the storm, the considered GOES and THEMIS data sets provide appropriate coverage at high L-shells with which to address this topic.

4.1. D_{LL} From THEMIS Satellites

Figure 3 shows ULF wave PSD as a function of time and frequency for perturbations in the electromagnetic fields measured by the THEMIS-A, THEMIS-D, and THEMIS-E satellites. We show inbound and outbound passes of THEMIS-A, THEMIS-D, and THEMIS-E probes on each panel of the plot designating them with different colors. Data from the THEMIS-A satellite are shown in Figure 3, and throughout the paper, with a red background and red-colored labels. Meanwhile, green color represents THEMIS-E, and blue color represents THEMIS-D; the labels on the top of each plot also designate different probes (A, D, or E) and distinguish between their inbound (in) and outbound (out) passes. Note that we show only the time period between
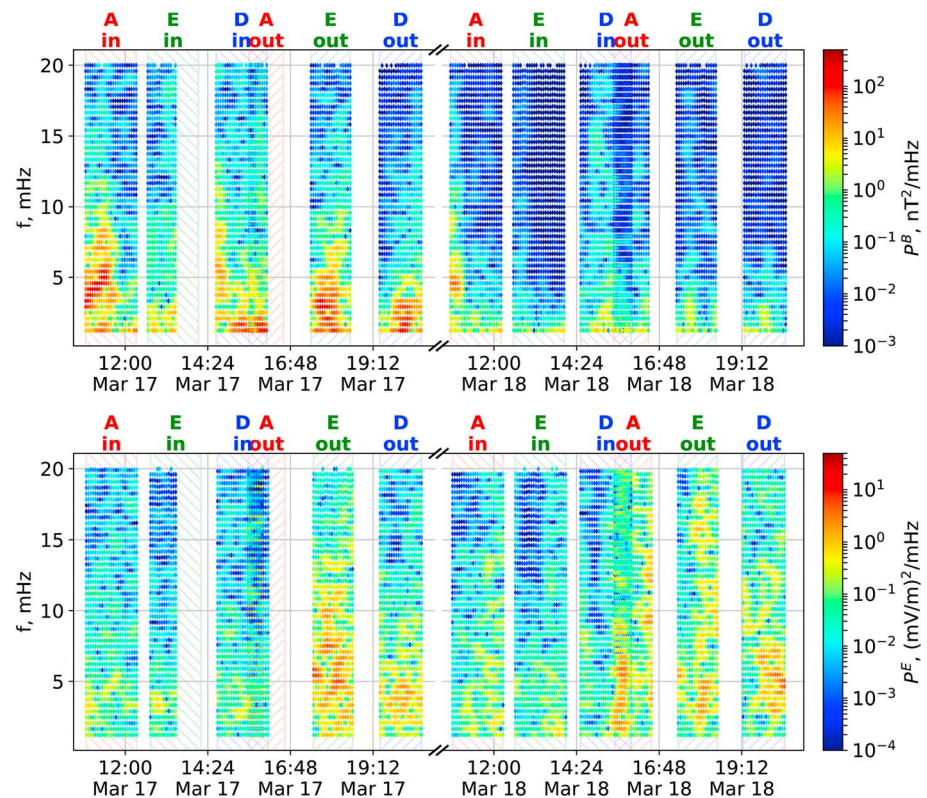
Figure 3. Spectrograms of ultralow frequency perturbations in the compressional component of the magnetic field $B_\parallel$ (top panel) and the quasi-azimuthal component of the electric field E_ϕ (bottom panel) measured by the THEMIS satellites from 10:30 till 21:00 UT on both 17 and 18 March 2015. The soft highlighted background in red indicates data obtained from THEMIS-A satellite, the blue color corresponds to THEMIS-E, and the green color corresponds to THEMIS-D. Note that we show inbound and outbound passes of all three satellites on the same plot and label them above each panel "in" or "out," respectively. Also note that the inbound pass of THEMIS-D overlaps with the outbound pass of THEMIS-A at around 15:00 UT. Times when the data are absent for THEMIS-E and when THEMIS-A is in the magnetosheath are not shown on the plot. THEMIS = Time History of Events and Macroscale Interactions during Substorms.

10:30 and 21:00 UT for both 17 and 18 March, breaking the *x* axis between two periods. THEMIS satellites spend only ~10 hr/day in the outer radiation belt, and this representation makes the presentation clearer. Also, note that the time dependence of the PSD, and the D_{LL} coefficients later in the text, also incorporate the L-shell dependence due to the movement of the spacecraft along the orbit.

The top panel of Figure 3 shows a spectrogram of ULF wave PSD in the compressional component of the magnetic field (P^B). A relatively large PSD $\gtrsim$10 nT^2/mHz is present for frequencies ≤5 mHz during the main phase of the storm on 17 March. Figure 3 shows that during the progression of the UT day on 17 March, the substantial compressional power is bounded by a frequency, which subsides from 10 mHz, as measured during an inbound pass of THEMIS-A, to 3 mHz toward the end of the main phase at the end of the UT day on 17 March, as measured during an outbound pass of THEMIS-D. The majority of the compressional wave power is confined to low frequencies of <3 mHz during the first day of the recovery phase on 18 March. Meanwhile, the bottom panel of Figure 3 shows that the wave power in the quasi-azimuthal component of the electric field is spread over a large frequency range. Unlike the PSD of the magnetic component, P^E shows a strong magnetic local time dependence. Low values of $P^E \leq$ 0.5 (mV/m)^2/mHz are, in general, present on the duskside during the inbound passes of the THEMIS probes. Meanwhile, relatively large values of $P^E \geq$ 0.5 (mV/m)^2/mHz are present in the noon sector as measured during the outbound passes of the THEMIS satellites. Additionally, there is no significant change in the PSD for the E_ϕ component between the main phase and the recovery phase of the storm in the noon sector (at ~15:00–21:00 UT). During the recovery phase the P^E power spectra show some evidence of the frequency independence consistent with
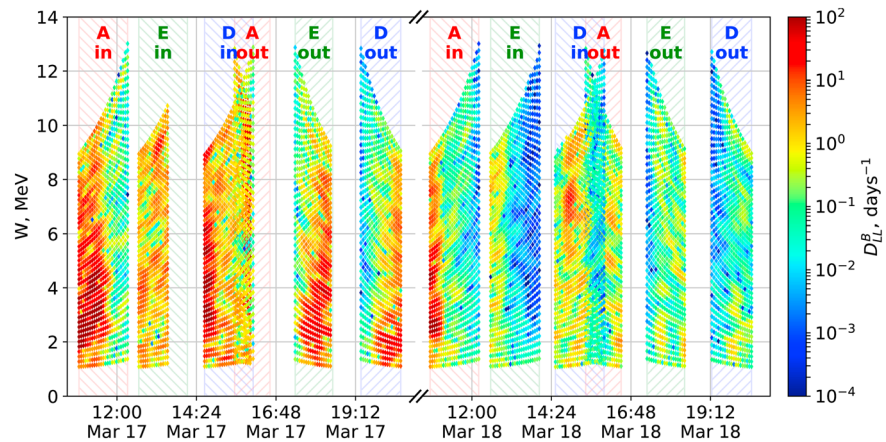
Figure 4. D^B_{LL} as a function of time and energy using local measurements of compressional ultralow frequency wave power spectral density P^B recorded by THEMIS-A, THEMIS-D, and THEMIS-E. Drift ($m = 1$) resonance and a dipole magnetic field are assumed and D^B_{LL} is calculated using the Fei et al. (2006) formulas. The color scheme for this plot is the same as in Figure 3. The energy dependence was obtained by calculating the drift resonance ($m = 1$) electron energy for the waves in the frequency range from 1.2 to 20 mHz. See text for more detail. THEMIS = Time History of Events and Macroscale Interactions during Substorms.

the Kp-dependent empirical statistical models (e.g., Ozeke et al., 2014). In the main phase, however, the spectra appear to be dominated by the power below 10 mHz.

There are two time regions missing in Figure 3 when the data have no correct physical interpretation from the point of the radial diffusion or absent. The first one, during the outbound pass of THEMIS-A on 17 March (from 16:00 until 16:30 UT), when THEMIS-A had crossed the magnetopause and was outside the magnetosphere. The second, during the inbound pass of THEMIS-E on 17 March (from 13:30 until 14:00 UT), during which THEMIS-E has no electric field measurements. Therefore, these two regions are ignored in the subsequential analysis.

Figure 4 shows the D^B_{LL} coefficient calculated using equation (2b), where $P^B(L, f)$ is taken using data from the top panel of Figure 3. Figure 4 shows the value of the D^B_{LL} coefficient as a function of total electron energy, W, and time. The energy dependence is obtained by using the previous assumption that $m = 1$ and therefore that the wave angular frequency $\omega = 2\pi f$ is the same as the drift frequency ω_d of an electron. Because ω_d is a function of the relativistic energy of a particle, we use a transformation between wave frequency, f in hertz, and energy, W in megaelectron volts, in the form of equation (4), where

$$W = \frac{m_e c^2}{2} \left(\frac{2}{3} \frac{C_d f}{L} + \sqrt{\frac{4}{9} \frac{C_d^2 f^2}{L^2} + 4} \right), \tag{3}$$

and $m_e c^2 = 0.511$ MeV is the rest mass of an electron in units of energy, and C_d is a numerically obtained coefficient and is equal to $1.557 \cdot 10^4$ s for electrons (Walt, 1994). We further only consider particles with 90° equatorial pitch angle. The same approach is used to analyze the D^E_{LL} coefficients shown in Figure 5.

Figures 4 and 5 show that both the D^B_{LL} and D^E_{LL} coefficients behave coherently as a function of energy during this interval; that is, the magnitudes of the diffusion coefficients as determined using local field measurements from THEMIS indicate much larger changes happening as a function of time and position than as a function of energy. Consistent with prior statistical models (e.g., Ozeke et al., 2014), both D^B_{LL} and D^E_{LL} have a strong L-shell dependence with larger magnitudes on the higher L-shells. However, some energy-dependent features most likely associated with the ULF wave packets still exist. For example, during the end of the outbound pass of THEMIS-A on 18 March the magnetic diffusion D^B_{LL} is enhanced at a series of particular energies. This is consistent with encountering a short-lived ULF wave packet that is localized in frequency. Additionally, Figure 5 shows signs of a weak energy dependence during the main phase of the storm with higher D^E_{LL} at lower energies. This dependence becomes less apparent during the recovery phase on 18 March where the electric diffusion coefficient shows a much more coherent behavior across different energies. Nonetheless, the energy dependence of D^E_{LL} is in general weaker than the dependence on time or
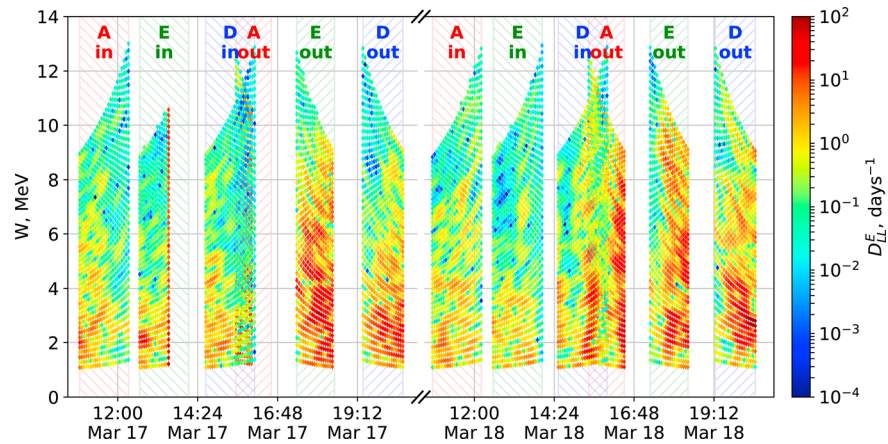
Figure 5. D_{LL}^E as a function of time and energy using local measurements of quasi-azimuthal ultralow frequency wave power spectral density P^E recorded by THEMIS-A, D, and E. The same format as Figure 4. THEMIS = Time History of Events and Macroscale Interactions during Substorms.

position. The same conclusion can also be made about D_{LL}^B; note, however, unlike D_{LL}^E, D_{LL}^B is much larger in the main phase than in the recovery phase. Similar to the behavior of P^E, the D_{LL}^E coefficient is enhanced in the noon-dawn sector in comparison to the measurements from the dusk sector. It again reinforces the importance of including local time dependence in future radial diffusion parametrizations.

Overall, this demonstrates that during the 17–18 March storm the observed power spectral densities near the equatorial plane at THEMIS altitudes generate D_{LL}^E and D_{LL}^B coefficients that are largely coherent across different energies. This can be compared to the case of statistical Kp-dependent models for D_{LL}^E and D_{LL}^B derived from ULF wave power (e.g., Ozeke et al., 2014), which are energy independent. Our observations show that some variation with energy remains but appears to be less influential than changes in time or position. However, as described above, the statistical estimates are not the good representation for the rates of radial diffusion, especially during the main phase.

In order to compare the event-specific and statistical rates of diffusion, Figure 6 shows the averaged diffusion coefficients $\langle D_{LL}^B \rangle$ and $\langle D_{LL}^E \rangle$ generated using THEMIS ULF wave fields and calculating the mean D_{LL} from Figures 4 and 5 for energies from 1 to 13 MeV, which corresponds to PSD from 1.2 to 20 mHz at THEMIS altitudes in the equatorial plane. The event-specific D_{LL} coefficients calculated using THEMIS data are shown with colored lines. The color scheme is the same as in Figures 4 and 5: red for THEMIS-A, green for THEMIS-E, and blue for THEMIS-D. Diffusion coefficients calculated from the Ozeke et al. (2014) statistics and which are energy (frequency) independent are shown with black lines. Panel (a) of Figure 6 shows averaged $\langle D_{LL}^B \rangle$ coefficient, panel (b) shows averaged $\langle D_{LL}^E \rangle$ coefficient, panel (c) shows the ratio of $\langle D_{LL}^E \rangle$ over $\langle D_{LL}^B \rangle$, and panel (d) shows the total radial diffusion coefficient as the sum of the two, $\langle D_{LL}^E \rangle + \langle D_{LL}^B \rangle$.

Immediately obvious in the Figure 6 is that the event-specific D_{LL}^B coefficients (Figure 6a) appear to be larger than the Ozeke et al. (2014) coefficients by a factor of ~10 during the main phase of the storm on 17 March. However, during the recovery phase, toward the end of 18 March, the THEMIS-derived magnetic diffusion coefficients D_{LL}^B approach those in the Ozeke et al. (2014) statistics. Figure 1 shows that the IMF is strongly southward during the main phase, meanwhile, it oscillates around zero during the recovery phase. Note that the Ozeke et al. (2014) statistics are derived using Kp and all geomagnetic, both storm and nonstorm, conditions over a solar cycle. The existence of the strong southward IMF during the main phase of this intense storm may change the Kp dependence of the ULF wave power, resulting in the failure of Ozeke et al. (2014) statistical approach to accurately specify storm time D_{LL}^B coefficients during the main phase of the storm. At the same time, the electric diffusion coefficients (Figure 6b) are smaller than the Ozeke et al. (2014) statistics during the main phase of the storm but return to good agreement with the statistical model later during the recovery phase. Moreover, Figure 6c shows that during the main phase of the storm on 17 March the D_{LL}^B coefficients exceed D_{LL}^E by a factor of ~10. Meanwhile, the Ozeke et al. (2014) statistics predict the opposite relationship—that the D_{LL}^E coefficients should be larger than the D_{LL}^B coefficients almost by a factor of 100. In addition, Figure 6d shows that during the main phase of the storm the total radial
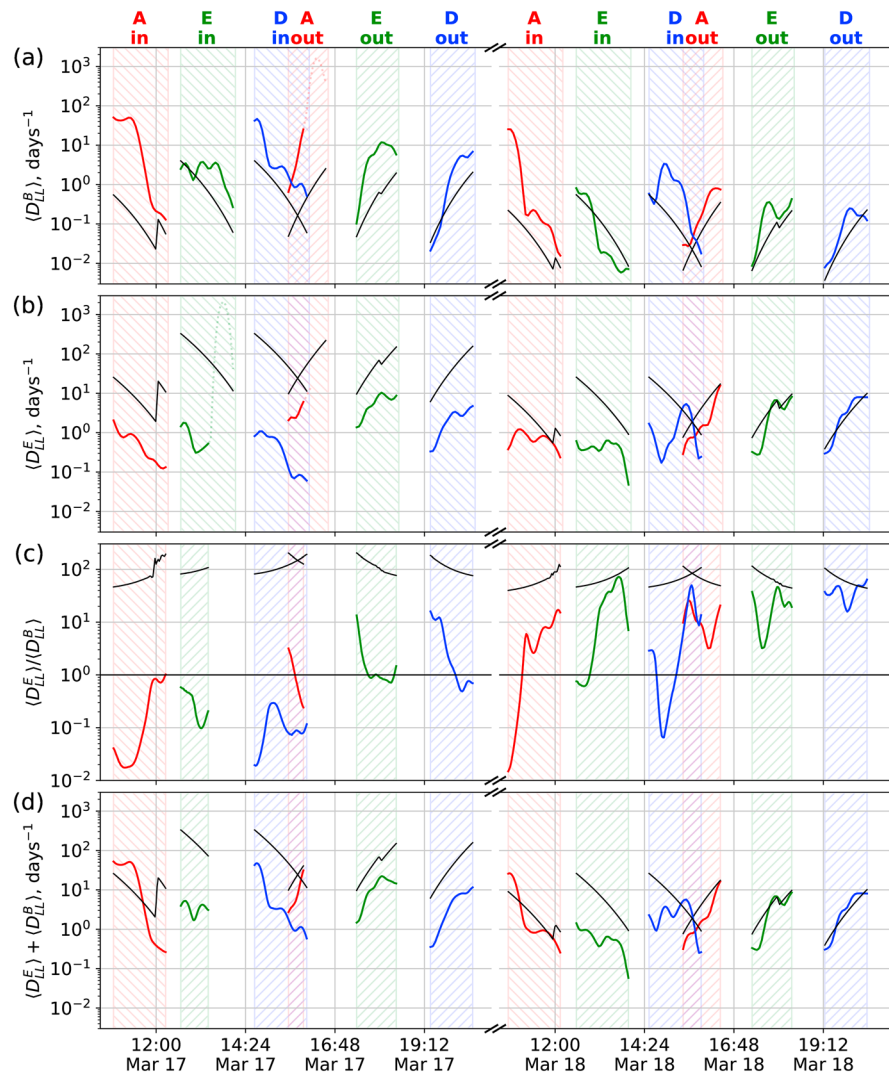
Figure 6. Radial diffusion coefficients, their ratio, and sum, calculated using local fields data from the THEMIS-A, THEMIS-D, and THEMIS-E satellites during the 17–18 March 2015 storm. The color scheme indicating data from each of THEMIS-A, THEMIS-D, and THEMIS-E satellites is the same as in Figure 3. The panels from top to bottom: (a) $\langle D_{LL}^B \rangle$, (b) $\langle D_{LL}^E \rangle$, (c) the ratio of $\langle D_{LL}^E \rangle / \langle D_{LL}^B \rangle$, and (d) the sum of diffusion coefficients $\langle D_{LL}^E \rangle + \langle D_{LL}^B \rangle$. In each panel, we additionally show the Ozeke et al. (2014) statistical diffusion coefficients expressed as a function of Kp at the time and L-shells of the THEMIS observations. THEMIS = Time History of Events and Macroscale Interactions during Substorms.

diffusion coefficient $D_{LL}=D_{LL}^E+D_{LL}^B$ calculated using the statistical Kp-parametrization mostly dominates over the data-driven result.

In the analysis of storm time and non–storm time ULF wave power, Dimitrakoudis et al. (2015) showed that the dependence of ULF wave power on Kp, derived during storm times, can be different from that obtained from statistics averaging across conditions from the whole solar cycle. However, the study of Dimitrakoudis et al. (2015) did not distinguish between the main phase and the recovery phase of the storm, relying only on the magnitude of Dst but not on its increasing or decreasing trend. Pokhotelov et al. (2016), in the analysis of the October 2012 storm, further showed that the main phase ULF wave power, especially as it relates to compressional disturbances and D_{LL}^B, can be significantly enhanced as compared to non-storm times. The event-specific results presented in this paper are consistent with these previous studies and indicate in particular that the rates of radial diffusion during the main phase of the storms may differ significantly from other times. As a result, Kp-dependent empirical specifications of radial diffusion coefficients should be used with care, especially during storm main phase—and radial transport such as to a compressed magnetopause
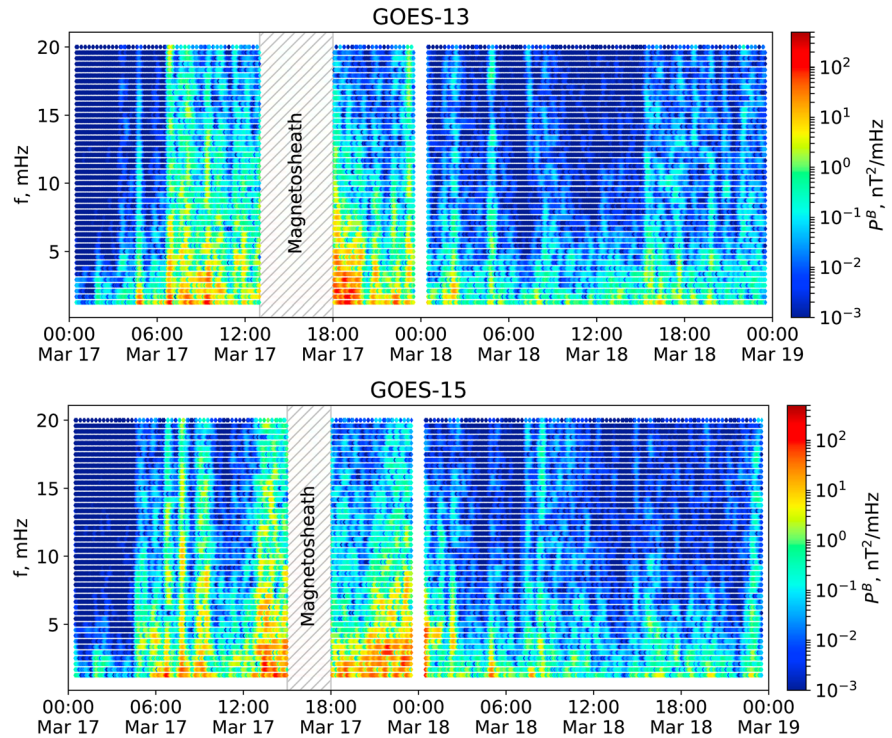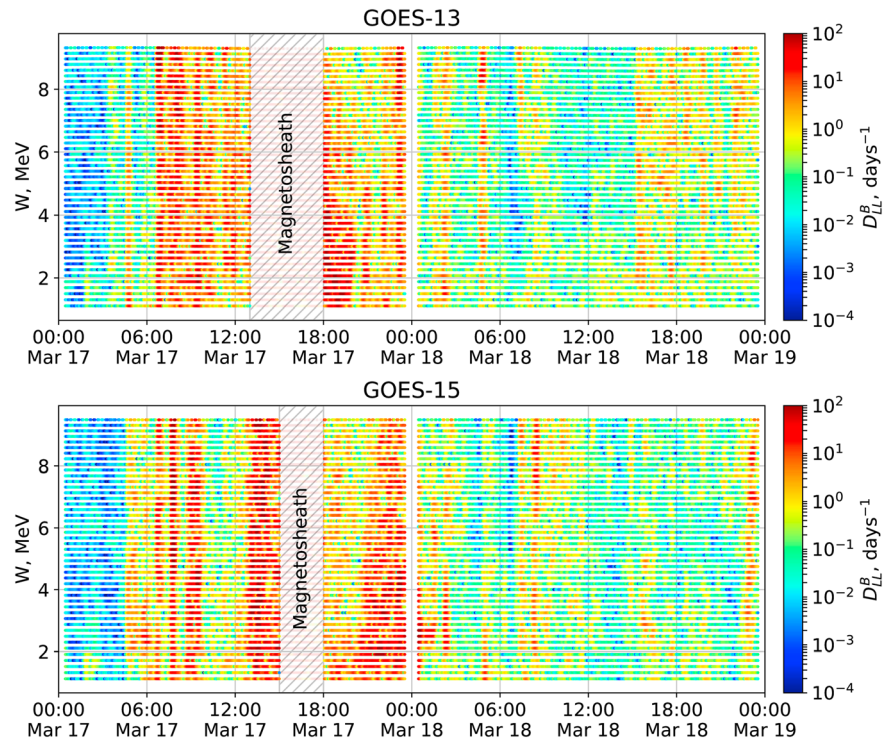
Figure 7. Spectrograms of ultralow frequency waves in the compressional component of the magnetic field as measured by the GOES-13 (top panel) and GOES-15 (bottom panel) spacecraft at geosynchronous orbit. Shaded regions indicate periods when GOES is in the magnetosheath (see text for details). GOES = Geostationary Operational Environment Satellite.

might be incorrectly represented using empirical Kp-dependent model during these times. In addition, the total radial diffusion coefficient ($D_{LL} = D_{LL}^E + D_{LL}^B$), according to the Ozeke et al. (2014) parametrization, reaches very high values of $D_{LL} \approx 100$ day^{-1} during 17 March. In comparison to a ~1 MeV electron drift period, such inferred fast timescales may not be consistent with the radial diffusion paradigm. Meanwhile, the data-derived total D_{LL} is ~10 day^{-1}, which still implies fast radial diffusion but is more consistent with the observed loss timescale. This observation again emphasizes the importance of either using event-based D_{LL} or improving the statistical models for the radial diffusion coefficients.

4.2. D_{LL}^B From GOES Satellites

Analogous to the analysis of the THEMIS data presented in the previous section, we show spectrograms of ULF perturbations in the compressional component of the magnetic field measured by GOES-13 and GOES-15 satellites in Figure 7. Similar to the THEMIS data analysis, we ignore periods when the satellites are inside the magnetosheath and where very large $P^B > 10^2$ nT^2/mHz of the magnetosheath turbulence across the whole frequency range are present in the spectrograms during these times. For GOES-13 (top panel of Figure 7) the spacecraft is in the sheath across a large fraction of the orbit on the dayside between 13:00 and 18:00 UT on 17 March. Meanwhile, for GOES-15 (bottom panel of Figure 7) the region when the spacecraft is in the sheath spreads from 15:00 until 18:00 UT on 17 March. These regions are not shown and marked as "Magnetosheath" in the subsequent GOES plots in this paper.

The region of relatively broadband waves with large P^B is present across the Pc4–Pc5 frequency range during the main phase of the storm, especially when there is a strong southward IMF. Figure 1 shows that there are two time periods when the IMF has a large southward component, in particular from 05:00 until 08:45 UT and from 12:00 until 24:00 UT on 17 March. These times correspond to times of large compressional, broadband wave spectra in P^B when a PSD of $\gtrsim 1$ nT^2/mHz is present at GOES-15 for frequencies > 5 mHz. The same characteristics are present for the GOES-13 data but are partially obscured by the magnetopause crossing. Additionally, the power spectral densities at both GOES-13 and GOES-15 subside to lower power levels during the recovery phase on 18 March when the B_z component of the IMF is small and fluctuates around 0.
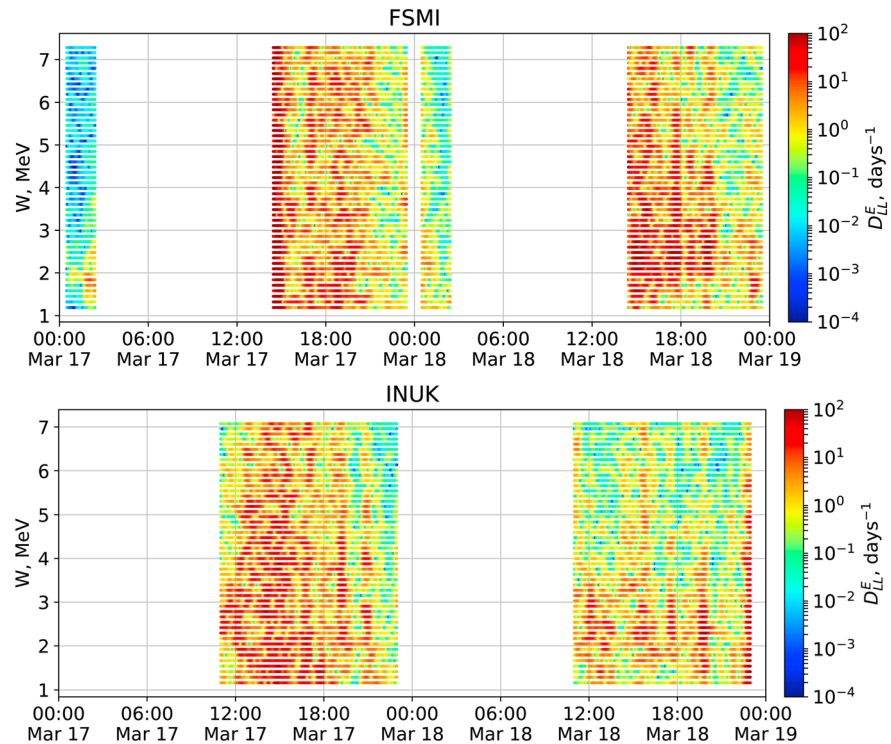
Figure 8. Diffusion coefficient D_{LL}^B as a function of time and drift ($m = 1$) resonating electron energy as calculated using the Fei et al. (2006) formulas using the observed compressional ultralow frequency wave power from Figure 7 for the GOES-13 (top panel) and GOES-15 (bottom panel) satellites. GOES = Geostationary Operational Environment Satellite.
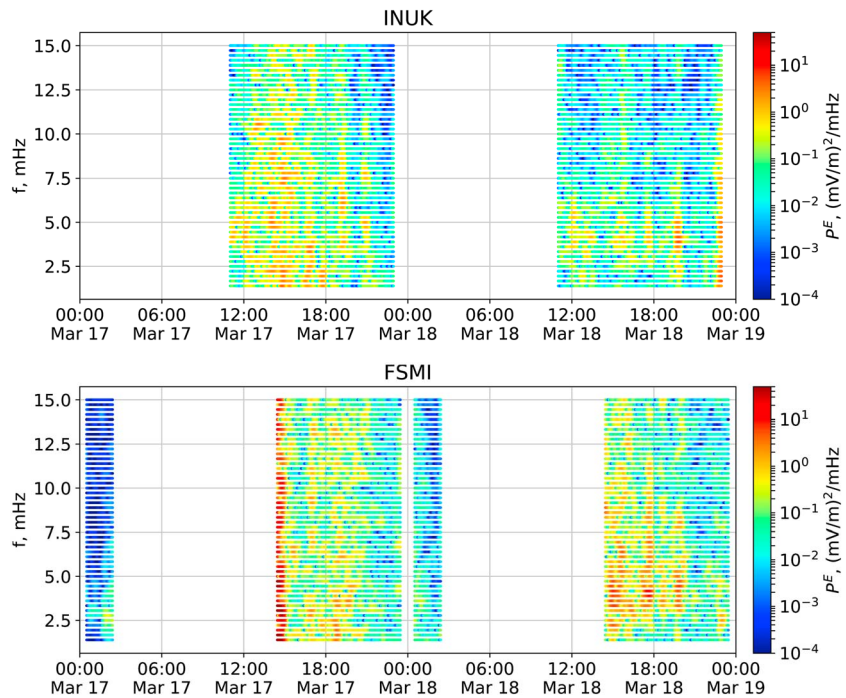
Figure 9. Spectrograms of ultralow frequency waves in the quasi-azimuthal component of the equatorial electric field as derived from a mapping of the D-component from the ground-based magnetometers at Inukjuak (INUK, top panel) and Fort Smith (FSMI, bottom panel).

Figure 10. D_{LL}^E electric diffusion coefficient as a function of time and drift ($m = 1$) resonant electron energy calculated using the Fei et al. (2006) formulas. The power spectral density of equatorial E_ϕ is obtained by mapping the D-component of the magnetic field on the ground to the equatorial plane using the Ozeke et al. (2009) technique. The top panel shows data corresponding to Inukjuak (INUK) magnetometer (close to magnetic conjugate to GOES-13), and the bottom panel shows data derived from Fort Smith (FSMI) magnetometer (close to GOES-15). GOES = Geostationary Operational Environment Satellite.

Figure 8 shows D_{LL}^B coefficients as a function of drift ($m = 1$) resonant particle energy and time for GOES-13 (top panel) and GOES-15 (bottom panel) derived from the compressional power spectral densities from 1.2 to 20 mHz shown in Figure 7. Similar to the analysis of the THEMIS data, GOES D_{LL}^B as a function of energy is calculated using the same frequency range as in Figure 7. Figure 8 shows that the D_{LL}^B coefficients at geostationary orbit again show a strong energy coherence. However, there are some limited time intervals during the recovery phase when D_{LL}^B is more enhanced at particular energies. Overall, the D_{LL}^B coefficients at GOES show even more coherent behavior across energies than indicated in THEMIS data, even though both data sets show much larger changes happening as a function of time than energy. Note that the regions when the GOES satellites are in the magnetosheath are again not shown in the plots. Moreover, even when the IMF turns southward and a broad PSD is observed for high frequencies ($f > 5$ mHz), the proportionality of $P^B \propto f^{-2}$ stays valid largely delivering an energy independence consistent with the Kp dependent empirical statistical models. Further analysis of the average values of the D_{LL}^B coefficients is presented in section 5 of the paper, where a comparison to the equatorial D_{LL}^E derived from ground-based magnetometer data is presented.

4.3. Equatorial D_{LL}^E Derived From Ground-Based Magnetometer Data

We obtain the quasi-azimuthal component of the electric field E_ϕ in the equatorial plane by mapping the D-component magnetic field measurements from selected ground-based magnetometers near the magnetic footprint of the GOES satellites. In this study, we use a magnetometer in Inukjuak (INUK) to map to E_ϕ near GOES-13. We use the Tsyganenko and Sitnov (2005) magnetic field model to determine that the INUK magnetometer from the AUTUMNX chain (Connors et al., 2016) is close to the footprint of the GOES-13 magnetic field line during 17–18 March 2015. Similarly, we used the Fort Smith magnetometer (FSMI) from the CARISMA array (Mann et al., 2008) for the determination of E_ϕ near GOES-15. The resulting spectrograms P^E as a function of frequency and time for both ground-based magnetometers are shown in Figure 9. Meanwhile, the resulting D_{LL}^E as a function of electron energy and time are shown in Figure 10, where the
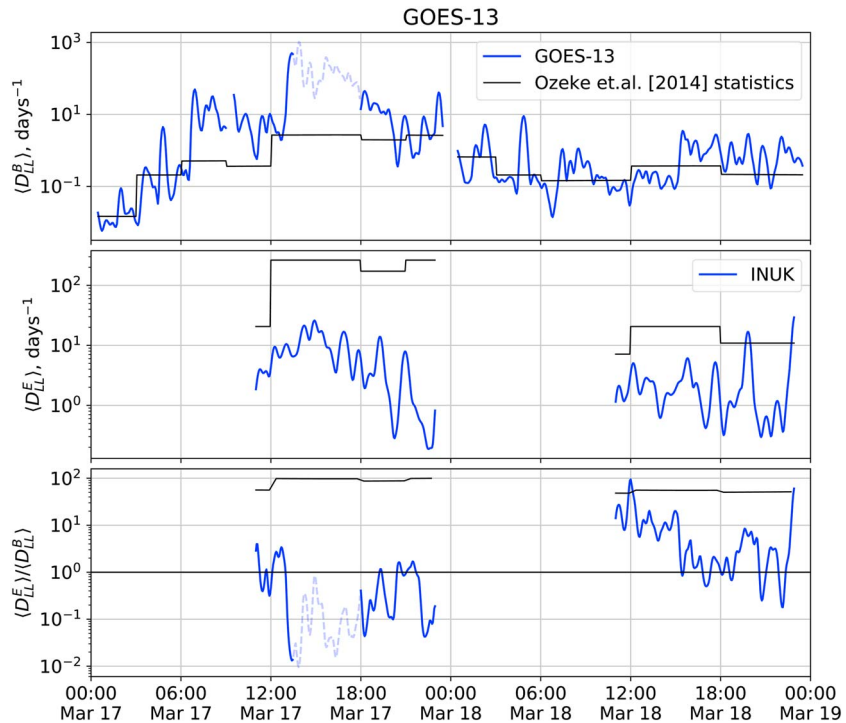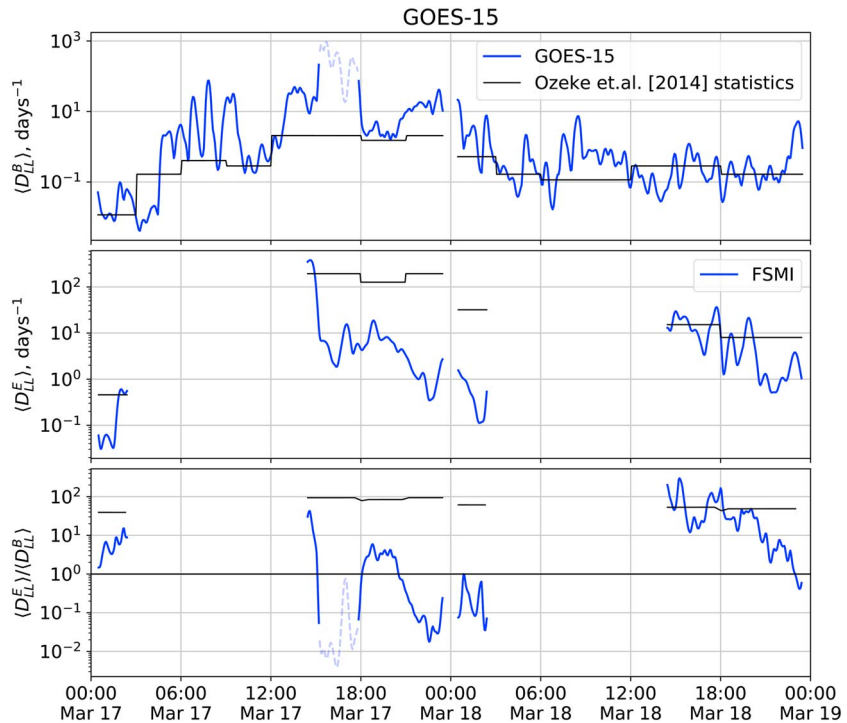
Figure 11. Comparison of various radial diffusion coefficients for 17–18 March 2015 storm at the locations of the GOES-13 satellite. In the top panel, the blue line represents $\langle D_{LL}^B \rangle$ data obtained using in situ GOES-13 magnetic observations, meanwhile the black line represents the (event independent) D_{LL}^B from the Ozeke et al. (2014) Kp statistics. The middle panel shows the average $\langle D_{LL}^E \rangle$ coefficient in blue obtained by mapping the D-component ultralow frequency wave power from the Inakjuak ground-based magnetometer to the equatorial plane, and the Ozeke et al. (2014) Kp-dependent statistical model in black. The bottom panel shows the ratio of $\langle D_{LL}^E \rangle$ and $\langle D_{LL}^B \rangle$ for both observational (blue) and Ozeke et al. (2014) Kp-dependent empirical model (black). See text for more details. GOES = Geostationary Operational Environment Satellite.

top plot corresponds to the Inukjuak station (INUK) and the bottom plot corresponds to Fort Smith station (FSMI). D_{LL}^E in Figure 10 was derived using magnetic D-component PSD for frequencies between 1.2 and 15 mHz, which correspond to electron energies from 1 to 7 MeV at geostationary orbit assuming drift ($m = 1$) resonance. Even though during the main phase some energy dependence in D_{LL}^E was inferred using THEMIS data, an interesting observation is that the D_{LL}^E derived from the ground are more energy independent. A slight energy dependence is present for the D_{LL}^E from INUK during the recovery phase, but this is not present for D_{LL}^E derived from FSMI data. Overall, D_{LL}^E derived from the ground-based magnetometer data show a relatively coherent behavior at different energies with much larger changes happening as a function of time.

4.4. Comparison of D_{LL}^E and D_{LL}^B at Geosynchronous Orbit

In the results presented here using in situ THEMIS electric and magnetic field data, it was clear that during the main phase of the 17–18 March 2015 storm the data-derived D_{LL}^B and D_{LL}^E coefficients had very different behavior than predicted by, for example, the empirical Kp-dependent diffusion coefficient model by Ozeke et al. (2014). The Ozeke et al. (2014) statistics, using only Kp as a fitting parameter and using data from the entire solar cycle appears, at least for this storm, to significantly overestimate D_{LL}^E and underestimate D_{LL}^B during the main phase. Instead of D_{LL}^E being ~100 times larger than D_{LL}^B, the THEMIS data imply that both diffusion coefficients are of the same magnitude, in agreement with prior results presented by Pokhotelov et al. (2016) using THEMIS and Van Allen Probes measurements for the October 2012 magnetic storm. To examine this relationship further, we also examine the relative magnitude of in situ $\langle D_{LL}^B \rangle$ as derived from GOES magnetometer data and $\langle D_{LL}^E \rangle$ as derived by mapping data from magnetically conjugate ground-based magnetometers to the equatorial plane, proximal to the GOES satellites. Figure 11 shows a comparison between the average radial diffusion coefficients $\langle D_{LL}^B \rangle$ derived from GOES-13 magnetometer, corresponding $\langle D_{LL}^E \rangle$ derived from the INUK ground-based magnetometer, and the Ozeke et al. (2014) statistics on

Figure 12. Comparison of the radial diffusion coefficients for data from GOES-15 satellite and Fort Smith ground-based magnetometer during 17–18 March 2015 storm. The same format as Figure 11. GOES = Geostationary Operational Environment Satellite.

the geosynchronous orbit. Figure 12 shows the same comparison between these diffusion coefficients at geosynchronous orbit near GOES-15.

Consistent with the results from the THEMIS satellites (Figure 6), the radial diffusion coefficients at geosynchronous orbit show the same discrepancy between storm specific and statistically expected D_{LL} values during the main phase of the storm. In particular, the D_{LL}^B coefficients from the in situ GOES measurements are larger than those predicted by the Ozeke et al. (2014) Kp-parameterization by almost a factor of 100 during the main phase of the storm (top panels of Figures 11 and 12). Meanwhile, the mapped D_{LL}^E coefficients derived from the ground-based magnetometer data are smaller than Ozeke et al. (2014) statistics (middle panels of Figures 11 and 12). Also consistent with the in situ THEMIS data, during the main phase of the storm, the D_{LL}^B coefficients are of the same order of magnitude as D_{LL}^E. Therefore, the Ozeke et al. (2014) Kp-parameterization underestimates the relative importance of the D_{LL}^B coefficient (black lines in Figure 6c and the bottom panels of Figures 11 and 12) during the main phase. Hence, neglecting the magnetic diffusion in simulations, based purely on the behavior of any Kp-parameterization, may lead to an underestimation of the total radial transport during the main phase by a factor of 2 or more. Note, however, that particularly for this storm the statistical total diffusion coefficient obtained from the Ozeke et al. (2014) Kp-parameterization dominates over the data-derived one and has extremely large values $D_{LL}^E \approx 100$ day^{-1} (see the bottom panel of Figure 6 and the middle panels of Figures 11 and 12). This result again shows that Kp-parameterizations should be used with care especially during the main phase of very intense geomagnetic storms. Nonetheless, the storm-specific data-derived D_{LL}^E, D_{LL}^B, and their ratio are the same as predicted by the Ozeke et al. (2014) parametrization during the recovery phase on 18 March 2015.

5. Discussion and Conclusions

It is worthwhile to compare the results presented in this paper with similar studies of other magnetic storms and other prior approaches used to study the 17–18 March 2015 event. In particular, it is interesting to compare our calculations of power spectral densities with the results reported by Li et al. (2016, 2017). In their studies, Li et al. used the Lyon-Fedder-Mobarry (LFM) magnetohydrodynamic model to examine ULF perturbations in the magnetosphere and adapted the Fei et al. (2006) analytic approach to calculate the radial

diffusion coefficients in the simulation during the 17–18 March 2015 magnetic storm. Figure 5 of Li et al. (2016) shows spectrograms of P^E (their "E_Φ power") and P^B (their "B_Z power") as functions of frequency f and azimuthal wave number, m, during the prestorm and the main phase of the storm. Their LFM simulation showed that the power stored in perturbations with $m = 1$ is dominant and larger than for waves with $m \geq 2$ by more than two orders of magnitude. This result validates our approach of assuming $m = 1$ in this paper. Note, however, that especially during periods where the $m = 1$ assumption is violated our results may represent an estimation of a lower threshold of the storm-specific radial diffusion coefficients for example since the D_{LL}^B coefficient is proportional to m^2.

According to the GOES data presented in our Figure 7, the bandwidth of compressional PSD is larger than that reported by Li et al. (2016) in their simulation during the main phase of the storm at 12:30 UT. GOES measurements show that the difference between P^B at 1 mHz and P^B at 8 mHz is 1 order of magnitude. Meanwhile, the simulation by Li et al. (2016) shows a difference of almost 5 orders of magnitude. Similar broadband wave was observed on THEMIS-E inbound pass in Figure 3 at around the same time. However, during the recovery phase where the IMF $B_z \approx 0$ nT, the observed compressional PSD narrows and resembles results in Li et al. (2016) for the prestorm phase. This shows that the LFM model, at least in the resolution reported by Li et al. (2016), underestimates compressional PSD during the period of the strong southward IMF in the main phase. However, the same slight frequency dependence of P^E is observed in our analysis and the Li et al. simulations for $m = 1$ during the main phase of the storm.

Additionally, Li et al. (2016) calculated of the D_{LL}^B and D_{LL}^E coefficients for electrons with different first adiabatic invariants in their Figure 6. The Li et al.. results show that the magnetic radial diffusion coefficients in their simulations are independent of the first adiabatic invariant—a result consistent with the strong energy coherence of magnetic diffusion reported in this paper. Meanwhile, Li et al. report a slight energy dependence of the electric diffusion coefficients during the main phase of the storm which disappears when IMF $B_z \approx 0$ nT. Note that in our analysis of THEMIS data, which relies on the assumption that $m = 1$ rather than a spectrum of multiple m's considered by Li et al., the energy dependence of D_{LL}^E in the main phase is somewhat larger than reported by Li et al. (2016). Nonetheless, this energy dependence remains weaker than the time dependence, as was described above.

However, as in the Ozeke et al. (2014) Kp-dependent statistical model the D_{LL}^E remain larger than D_{LL}^B by 2 or 3 orders of magnitude in Li et al. (2016) simulations, depending on storm phase. In contrast, the D_{LL}^B obtained from THEMIS measurements in this paper are either larger than, or have the same magnitude as, D_{LL}^E during the main phase of the storm. A comparison of the in situ D_{LL}^B derived data from GOES satellites at geosynchronous orbit, and D_{LL}^E derived from ground-based magnetometer data, show the same behavior. Note that during the main phase of the storm on 17 March, $D_{LL}^B \approx 10^1$ day^{-1} at geosynchronous orbit according to our GOES data-driven calculations. Meanwhile, the LFM model estimates $D_{LL}^B \approx 10^{-2}$ day^{-1}. Overall, this further suggests that there are magnetospheric processes which are active in the main phase of intense geomagnetic storms during periods of strongly southward IMF, and which produce large in situ compressional ULF fields as observed here in THEMIS and GOES satellite data. However, such processes may not be well-represented in current MHD models such as LFM.

Analysis of in situ THEMIS data (Figure 6) shows estimate of D_{LL}^B within range from 10^0 to 10^1 day^{-1} depending on L-shell, while D_{LL}^E is between 10^{-1} and 10^0 day^{-1}, during the main phase of the storm. Therefore, according to the in situ THEMIS data, magnetic (D_{LL}^B) diffusion may dominate an electric diffusion (D_{LL}^E) during the storm main phase. The same is also true for the geostationary orbit when comparing data obtained in situ from the GOES satellites, and derived from ground-based magnetometer data (Figures 11 and 12). Meanwhile, the Kp-dependent Ozeke et al. (2014) model show an opposite picture with $D_{LL}^B \ll D_{LL}^E$. Note that the storm-specific D_{LL} coefficients reverse their ratio and are well repeated by the Ozeke et al. (2014) Kp-parametrization during the recovery phase at least on 18 March during this storm. These results show that the Ozeke et al. (2014) parametrization may fail to accurately describe the D_{LL} coefficients during storm main phase especially during intervals with a strong southward IMF component ($B_z \approx -20$ nT).

Overall, Pc4–Pc5 ULF waves may cause rapid (~2.5 hr) electron outward radial transport during the March 2015 geomagnetic storm. This provides a compelling potential mechanism for depleting electron outer radiation belt by transporting charged particles to the magnetopause. Olifer et al. (2018) showed that transport to the outer boundary can be examined in the context of an analysis of the dynamics of the LCDS. According to the analysis presented by Olifer et al. (2018), during the main phase of the storm on 17 March 2015

the separation in $L*$ between the LCDS and the heart of the radiation belt may only be around $\Delta L*=1$ (see Figure 3 of Olifer et al. (2018)). According to the radial diffusion paradigm, such a separation can be easily bridged by fast outward radial diffusion. Additionally, in this paper, we demonstrate that the storm-specific radial diffusion coefficients may be largely energy independent. This agrees nicely with the results of Olifer et al. (2018) (e.g., their Figure S2 in the supporting information) where it was shown that the loss patterns and LCDS dynamics are not only closely related but also similar across a wide range of energies during the March 2015 storm.

As mentioned above, it is interesting to compare our results with those of Pokhotelov et al. (2016) where a similar analysis of D_{LL} coefficients was performed for the 8–9 October 2012 geomagnetic storm using THEMIS and Van Allen Probes data. Pokhotelov et al. report similar features whereby the radial diffusion coefficients demonstrate the characteristics that $D_{LL}^B \sim D_{LL}^E$ during the main phase of that storm and with a similar southward IMF ($B_z \approx -15$ nT). In the Pokhotelov et al. (2016) results, the Kp-dependent model overestimates D_{LL}^E by orders of magnitude as compared to the observations. Meanwhile, the event-specific D_{LL}^B is being underestimated by the Kp-parametrization in the statistical models by a factor of ~4. The behavior of the electric diffusion coefficient is similar to that which we report in this paper for the 17–18 March 2015 storm. However, the level of disagreement between data-driven and statistical D_{LL}^B is much higher for this event. One difference between the October 2012 storm and the March 2015 event studied here is that the latter was much more intense in terms of ring current dynamics with SYM-H index reaching -225 nT as compared to -120 nT during the October 2012 storm. In addition, the March 2015 storm has more strongly southward IMF conditions ($B_z \approx -20$ nT) than observed during the October 2012 storm ($B_z \approx -15$ nT). If the strong compressional disturbances observed during the March 2015 storm are driven by processes associated with strongly southward IMF then this might explain the discrepancy. Consistent with this hypothesis, very recent analysis of 15 years of ground-based magnetometer data by Bentley et al. (2018) showed a strong connection between enhanced ULF wave power and the magnitude of the southward component of the IMF. For example, their Figure 6 shows that the well-known increase of ULF wave power with increasing solar wind speed is significantly further enhanced by increasingly negative B_z.

In summary, and overall, our analysis of data-driven radial diffusion coefficients shows that the relative magnitudes of D_{LL}^E and D_{LL}^B may be significantly different during storm main phase than at other times. For example, using in situ THEMIS and GOES data, we show that during the main phase of the intense March 2015 storm the radial diffusion coefficients are not well described by the Ozeke et al. (2014) empirical Kp-dependent model. First, the D_{LL}^B coefficient is underestimated by the Kp-parametrization. Second, the solar cycle derived Kp statistics imply that the D_{LL}^B should be negligibly small in comparison to D_{LL}^E. However, during the main phase of the March 2015 storm, the event-specific results show different behavior with $D_{LL}^E \lesssim D_{LL}^B$. Thus, using the Ozeke et al. (2014) parametrization to represent the diffusion coefficients for radial diffusion simulations may lead to an incorrect representation of the total D_{LL} coefficient during the main phase. This suggests that there is an urgent need to produce new statistical models for D_{LL} coefficients during the main phase of a storm, perhaps including the influence of processes active during southward IMF. Providing more accurate radial transport models, especially for example during intense radiation belt extinction events (e.g., Olifer et al., 2018; Ozeke et al., 2017) may help to improve the accuracy of the magnetopause shadowing losses predicted by radial diffusion models. Understanding the relative contributions of fast outward radial diffusion to the LCDS, and therefore magnetopause shadowing, and local wave-particle scattering losses to the atmosphere, remains a major challenge for improving the accuracy of the radiation belt modeling. Improved future characterizations of especially the compressional disturbances that increase main phase D_{LL}^B in radiation belt simulations could help significantly in that regard.

References

Albert, J. M. (2005). Evaluation of quasi-linear diffusion coefficients for whistler mode waves in a plasma with arbitrary density ratio. *Journal of Geophysical Research*, *110*, A03218. https://doi.org/10.1029/2004JA010844

Angelopoulos, V. (2008). The THEMIS Mission. *Space Science Reviews*, *141*(1-4), 5–34. https://doi.org/10.1007/s11214-008-9336-1

Auster, H. U., Glassmeier, K. H., Magnes, W., Aydogar, O., Baumjohann, W., Constantinescu, D., et al. (2008). The THEMIS fluxgate magnetometer. *Space Science Reviews*, *141*(1), 235–264. https://doi.org/10.1007/s11214-008-9365-9

Baker, D. N., Kanekal, S. G., Hoxie, V. C., Batiste, S., Bolton, M., Li, X., et al. (2013). The Relativistic Electron-Proton Telescope (REPT) instrument on board the Radiation Belt Storm Probes (RBSP) spacecraft: Characterization of earth's radiation belt high-energy particle populations. *Space Science Reviews*, *179*(1), 337–381. https://doi.org/10.1007/s11214-012-9950-9

Bentley, S. N., Watt, C. E. J., Owens, M. J., & Rae, I. J. (2018). ULF wave activity in the magnetosphere: Resolving solar wind interdependencies to identify driving mechanisms. *Journal of Geophysical Research: Space Physics*, *123*, 2745–2771. https://doi.org/10.1002/2017JA024740

Bonnell, J. W., Mozer, F. S., Delory, G. T., Hull, A. J., Ergun, R. E., Cully, C. M., et al. (2008). The electric field instrument (EFI) for THEMIS. *Space Science Reviews*, *141*(1), 303–341. https://doi.org/10.1007/s11214-008-9469-2

Brautigam, D. H. (2005). CRRES electric field power spectra and radial diffusion coefficients. *Journal of Geophysical Research*, *110*, A02214. https://doi.org/10.1029/2004JA010612

Brautigam, D. H., & Albert, J. M. (2000). Radial diffusion analysis of outer radiation belt electrons during the October 9, 1990, magnetic storm. *Journal of Geophysical Research*, *105*(A1), 291–309. https://doi.org/10.1029/1999JA900344

Brito, T., Hudson, M. K., Kress, B., Paral, J., Halford, A., Millan, R., & Usanova, M. (2015). Simulation of ULF wave-modulated radiation belt electron precipitation during the 17 March 2013 storm. *Journal of Geophysical Research: Space Physics*, *120*, 3444–3461. https://doi.org/10.1002/2014JA020838

Brizard, A. J., & Chan, A. A. (2001). Relativistic bounce-averaged quasilinear diffusion equation for low-frequency electromagnetic fluctuations. *Physics of Plasmas*, *8*(11), 4762–4771. https://doi.org/10.1063/1.1408623

Connors, M., Schofield, I., Reiter, K., Chi, P. J., Rowe, K. M., & Russell, C. T. (2016). The AUTUMNX magnetometer meridian chain in Québec, Canada. *Earth, Planets and Space*, *68*(1), 2. https://doi.org/10.1186/s40623-015-0354-4

Dimitrakoudis, S., Mann, I. R., Balasis, G., Papadimitriou, C., Anastasiadis, A., & Daglis, I. A. (2015). Accurately specifying storm-time ULF wave radial diffusion in the radiation belts. *Geophysical Research Letters*, *42*, 5711–5718. https://doi.org/10.1002/2015GL064707

Drozdov, A. Y., Shprits, Y. Y., Usanova, M. E., Aseev, N. A., Kellerman, A. C., & Zhu, H. (2017). EMIC wave parameterization in the long-term VERB code simulation. *Journal of Geophysical Research: Space Physics*, *122*, 8488–8501. https://doi.org/10.1002/2017JA024389

Fei, Y., Chan, A. A., Elkington, S. R., & Wiltberger, M. J. (2006). Radial diffusion and MHD particle simulations of relativistic electron transport by ULF waves in the September 1998 storm. *Journal of Geophysical Research*, *111*, A12209. https://doi.org/10.1029/2005JA011211

Fraser, B., Morley, S., Grew, R., & Singer, H. (2013). Classification of Pc1-2 Electromagnetic Ion Cyclotron waves at geosynchronous orbit. In *Dynamics of the Earth's radiation belts and inner magnetosphere* (pp. 53–68). Washington, DC: American Geophysical Union. https://doi.org/10.1029/2012GM001353

Friedel, R., Reeves, G., & Obara, T. (2002). Relativistic electron dynamics in the inner magnetosphere—A review. *Journal of Atmospheric and Solar-Terrestrial Physics*, *64*(2), 265–282. https://doi.org/10.1016/S1364-6826(01)00088-8, sTEP-Results, Applications and Modelling Phase (S-RAMP).

Horne, R. B., Thorne, R. M., Glauert, S. A., Albert, J. M., Meredith, N. P., & Anderson, R. R. (2005). Timescale for radiation belt electron acceleration by whistler mode chorus waves. *Journal of Geophysical Research*, *110*, A03225. https://doi.org/10.1029/2004JA010811

Kang, S.-B., Fok, M.-C., Glocer, A., Min, K.-W., Choi, C.-R., Choi, E., & Hwang, J. (2016). Simulation of a rapid dropout event for highly relativistic electrons with the RBE model. *Journal of Geophysical Research: Space Physics*, *121*, 4092–4102. https://doi.org/10.1002/2015JA021966

Kersten, T., Horne, R. B., Glauert, S. A., Meredith, N. P., Fraser, B. J., & Grew, R. S. (2014). Electron losses from the radiation belts caused by EMIC waves. *Journal of Geophysical Research: Space Physics*, *119*, 8820–8837. https://doi.org/10.1002/2014JA020366

King, J. H. (2005). Solar wind spatial scales in and comparisons of hourly Wind and ACE plasma and magnetic field data. *Journal of Geophysical Research*, *110*, A02104. https://doi.org/10.1029/2004JA010649

Lee, J., Min, K., & Kim, K. (2013). Characteristic dimension of electromagnetic ion cyclotron wave activity in the magnetosphere. *Journal of Geophysical Research: Space Physics*, *118*, 1651–1658. https://doi.org/10.1002/jgra.50242

Li, Z., Hudson, M., Paral, J., Wiltberger, M., & Turner, D. (2016). Global ULF wave analysis of radial diffusion coefficients using a global MHD model for the 17 March 2015 storm. *Journal of Geophysical Research: Space Physics*, *121*, 6196–6206. https://doi.org/10.1002/2016JA022508

Li, Z., Hudson, M., Patel, M., Wiltberger, M., Boyd, A., & Turner, D. (2017). ULF wave analysis and radial diffusion calculation using a global MHD model for the 17 March 2013 and 2015 storms. *Journal of Geophysical Research: Space Physics*, *122*, 7353–7363. https://doi.org/10.1002/2016JA023846

Li, W., Thorne, R. M., Ma, Q., Ni, B., Bortnik, J., Baker, D. N., et al. (2014). Radiation belt electron acceleration by chorus waves during the 17 March 2013 storm. *Journal of Geophysical Research: Space Physics*, *119*, 4681–4693. https://doi.org/10.1002/2014JA019945

Loto'aniu, T. M., Singer, H. J., Waters, C. L., Angelopoulos, V., Mann, I. R., Elkington, S. R., & Bonnell, J. W. (2010). Relativistic electron loss due to ultralow frequency waves and enhanced outward radial diffusion. *Journal of Geophysical Research*, *115*, A12245. https://doi.org/10.1029/2010JA015755

Mann, I. R., Milling, D. K., Rae, I. J., Ozeke, L. G., Kale, A., Kale, Z. C., et al. (2008). The upgraded CARISMA magnetometer array in the THEMIS Era. *Space Science Reviews*, *141*(1), 413–451. https://doi.org/10.1007/s11214-008-9457-6

Mann, I. R., & Ozeke, L. G. (2016). How quickly, how deeply, and how strongly can dynamical outer boundary conditions impact Van Allen radiation belt morphology? *Journal of Geophysical Research: Space Physics*, *121*, 5553–5558. https://doi.org/10.1002/2016JA022647

Mann, I. R., Ozeke, L. G., Murphy, K. R., Claudepierre, S. G., Turner, D. L., Baker, D. N., et al. (2016). Explaining the dynamics of the ultra-relativistic third Van Allen radiation belt. *Nature Physics*, *12*, 978–983. https://doi.org/10.1038/nphys3799

Morley, S. K., Friedel, R. H. W., Cayton, T. E., & Noveroske, E. (2010). A rapid, global and prolonged electron radiation belt dropout observed with the Global Positioning System constellation. *Geophysical Research Letters*, *37*, L06102. https://doi.org/10.1029/2010GL042772

Morley, S. K., Koller, J., Welling, D. T., Larsen, B. A., Henderson, M. G., & Niehof, J. T. (2011). Spacepy—A python-based library of tools for the space sciences. In *Proceedings of the 9th Python in science conference (SciPy 2010)* (pp. 39–45). Austin, TX.

Morley, S. K., Sullivan, J. P., Carver, M. R., Kippen, R. M., Friedel, R. H. W., Reeves, G. D., & Henderson, M. G. (2017). Energetic particle data from the Global Positioning System constellation. *Space Weather*, *15*, 283–289. https://doi.org/10.1002/2017sw001604

Morley, S. K., Sullivan, J. P., Henderson, M. G., Blake, J. B., & Baker, D. N. (2016). The Global Positioning System constellation as a space weather monitor: Comparison of electron measurements with Van Allen Probes data. *Space Weather*, *14*, 76–92. https://doi.org/10.1002/2015sw001339

Olifer, L., Mann, I. R., Morley, S. K., Ozeke, L. G., & Choi, D. (2018). On the role of last closed drift shell dynamics in driving fast losses and Van Allen radiation belt extinction. *Journal of Geophysical Research: Space Physics*, *123*, 3692–3703. https://doi.org/10.1029/2018JA025190

Omura, Y., Furuya, N., & Summers, D. (2007). Relativistic turning acceleration of resonant electrons by coherent whistler mode waves in a dipole magnetic field. *Journal of Geophysical Research*, *112*, A06236. https://doi.org/10.1029/2006JA012243

Ozeke, L. G., Mann, I. R., Murphy, K. R., Rae, J. I., & Milling, D. K. (2014). Analytic expressions for ULF wave radiation belt radial diffusion coefficients. *Journal of Geophysical Research: Space Physics*, *119*, 1587–1605. https://doi.org/10.1002/2013JA019204

Ozeke, L. G., Mann, I. R., Murphy, K. R., Sibeck, D. G., & Baker, D. N. (2017). Ultra-relativistic radiation belt extinction and ULF wave radial diffusion: Modeling the September 2014 extended dropout event. *Geophysical Research Letters*, *44*, 2624–2633. https://doi.org/10.1002/2017GL072811

Ozeke, L. G., Mann, I. R., & Rae, J. I. (2009). Mapping guided Alfven wave magnetic field amplitudes observed on the ground to equatorial electric field amplitudes in space. *Journal of Geophysical Research*, *114*, A01214. https://doi.org/10.1029/2008JA013041

Pokhotelov, D., Rae, I. J., Murphy, K. R., Mann, I. R., & Ozeke, L. (2016). Effects of ULF wave power on relativistic radiation belt electrons: 8-9 October 2012 geomagnetic storm. *Journal of Geophysical Research: Space Physics*, *121*, 11,766–11,779. https://doi.org/10.1002/2016JA023130

Rae, I. J., Murphy, K. R., Watt, C. E. J., Halford, A. J., Mann, I. R., Ozeke, L. G., et al. (2018). The role of localized compressional ultra-low frequency waves in energetic electron precipitation. *Journal of Geophysical Research: Space Physics*, *123*, 1900–1914. https://doi.org/10.1002/2017JA024674

Schiller, Q., Tu, W., Ali, A. F., Li, X., Godinez, H. C., Turner, D. L., et al. (2016). Simultaneous event-specific estimates of transport, loss, and source rates for relativistic outer radiation belt electrons. *Journal of Geophysical Research: Space Physics*, *122*, 3354–3373. https://doi.org/10.1002/2016JA023093

Shprits, Y. Y., Drozdov, A. Y., Spasojevic, M., Kellerman, A. C., Usanova, M. E., Engebretson, M. J., et al. (2016). Wave-induced loss of ultra-relativistic electrons in the Van Allen radiation belts. *Nature Communications*, *7*, 12883. https://doi.org/10.1038/ncomms12883

Shprits, Y. Y., Meredith, N. P., & Thorne, R. M. (2007). Parameterization of radiation belt electron loss timescales due to interactions with chorus waves. *Geophysical Research Letters*, *34*, L11110. https://doi.org/10.1029/2006GL029050

Shprits, Y. Y., Subbotin, D. A., Meredith, N. P., & Elkington, S. R. (2008). Review of modeling of losses and sources of relativistic electrons in the outer radiation belt II: Local acceleration and loss. *Journal of Atmospheric and Solar-Terrestrial Physics*, *70*(14), 1694–1713. https://doi.org/10.1016/j.jastp.2008.06.014, dynamic Variability of Earth's Radiation Belts.

Shprits, Y. Y., Thorne, R. M., Friedel, R., Reeves, G. D., Fennell, J., Baker, D. N., & Kanekal, S. G. (2006). Outward radial diffusion driven by losses at magnetopause. *Journal of Geophysical Research*, *111*, A11214. https://doi.org/10.1029/2006JA011657

Shue, J.-H., Song, P., Russell, C. T., Steinberg, J. T., Chao, J. K., Zastenker, G., et al. (1998). Magnetopause location under extreme solar wind conditions. *Journal of Geophysical Research*, *103*(A8), 17,691–17,700. https://doi.org/10.1029/98JA01103

Singer, H., Matheson, L., Grubb, R., Newman, A., & Bouwer, D. (1996). Monitoring space weather with the GOES magnetometers. In E. R. Washwell (Ed.), *GOES-8 and Beyond*. Denver, CO: SPIE. https://doi.org/10.1117/12.254077

Thébault, E., Finlay, C. C., Beggan, C. D., Alken, P., Aubert, J., Barrois, O., et al. (2015). International geomagnetic reference field: The 12th generation. *Earth, Planets and Space*, *67*(1), 79. https://doi.org/10.1186/s40623-015-0228-9

Thorne, R. M., Li, W., Ni, B., Ma, Q., Bortnik, J., Chen, L., et al. (2013). Rapid local acceleration of relativistic radiation-belt electrons by magnetospheric chorus. *Nature*, *504*(7480), 411–414. https://doi.org/10.1038/nature12889

Thorne, R. M., Smith, E. J., Burton, R. K., & Holzer, R. E. (1973). Plasmaspheric hiss. *Journal of Geophysical Research*, *78*(10), 1581–1596. https://doi.org/10.1029/JA078i010p01581

Tsyganenko, N. A., & Sitnov, M. I. (2005). Modeling the dynamics of the inner magnetosphere during strong geomagnetic storms. *Journal of Geophysical Research*, *110*, A03208. https://doi.org/10.1029/2004JA010798

Turner, D. L., Morley, S. K., Miyoshi, Y., Ni, B., & Huang, C.-L. (2013). Outer radiation belt flux dropouts: Current understanding and unresolved questions. In *Dynamics of the Earth's Radiation Belts and Inner Magnetosphere* (pp. 195–212). Washington, DC: American Geophysical Union. https://doi.org/10.1029/2012GM001310

Turner, D. L., Shprits, Y., Hartinger, M., & Angelopoulos, V. (2012). Explaining sudden losses of outer radiation belt electrons during geomagnetic storms. *Nature Physics*, *8*, 208–212.

Tuszewski, M., Cayton, T. E., Ingraham, J. C., & Kippen, R. M. (2004). Bremsstrahlung effects in energetic particle detectors. *Space Weather*, *2*, S10S01. https://doi.org/10.1029/2003SW000057

Van Allen, J. A., & Frank, L. A. (1959). Radiation Around the Earth to a Radial Distance of 107,400 km. *Nature*, *183*(430), 430–434. https://doi.org/10.1038/183430a0

Walt, M. (1994). *Introduction to geomagnetically trapped radiation*. Cambridge: Cambridge University Press. https://doi.org/10.1017/cbo9780511524981

Yu, Y., Koller, J., Zaharia, S., & Jordanova, V. (2012). L* neural networks from different magnetic field models and their applicability. *Space Weather*, *10*, 2014. https://doi.org/10.1029/2011SW000743